AsTe3: A novel crystalline semiconductor with ultralow thermal conductivity obtained by congruent crystallization from parent glass

Jean-Baptiste Vaney, Cédric Morin, Julie Carreaud, Christophe Candolfi, Andrea Piarristeguy, Mickael Bigot, Judith Monnier, Annie Pradel, Vivian Nassif, Gabriel Cuello, et al.

Journal of Alloys and Compounds 1004 (2024) 175918

Contents lists available at ScienceDirect

Journal of Alloys and Compounds

journal homepage: www.elsevier.com/locate/jalcom

$AsTe_3$: A novel crystalline semiconductor with ultralow thermal conductivity obtained by congruent crystallization from parent glass

Jean-Baptiste Vaney [a], Cédric Morin [b], Julie Carreaud [c], Christophe Candolfi [a], Andrea Piarristeguy [d], Mickael Bigot [d], Judith Monnier [b], Annie Pradel [d], Vivian Nassif [e], Gabriel Cuello [f], Petr Levinsky [g], Bertrand Lenoir [a], Sylvian Cadars [c], Assil Bouzid [c], Olivier Masson [c], Jean-Paul Laval [c], Julie Cornette [c], Maggy Colas [c], Eric Alleno [b], Gaelle Delaizir [c,*]

[a] Institut Jean Lamour, UMR 7198 CNRS – Université de Lorraine, Nancy, France
[b] Université Paris Est Créteil, CNRS, Institut de Chimie et des Matériaux Paris Est (ICMPE), UMR 7182, Thiais, France
[c] Institut de Recherche sur les Céramiques (IRCER), UMR CNRS 7315-Université de Limoges, France
[d] ICGM, Univ Montpellier, CNRS, ENSCM, Montpellier, France
[e] Institut Néel, Grenoble, France
[f] Institut Laue Langevin, Grenoble Cedex 9, France
[g] Faculty of Nuclear Sciences and Physical Engineering, Czech Technical University, Prague, Czech Republic

A B S T R A C T

The synthesis of novel narrow-band-gap semiconductors with ultralow thermal conductivity opens a pathway to the design of functional materials with high thermoelectric performance or with interesting optical sensitivity in the infrared range. Here, we report on the discovery of the novel crystalline binary $AsTe_3$ (c-$AsTe_3$) prepared by spark plasma sintering (SPS) from full and congruent crystallization of amorphous $AsTe_3$ (a-$AsTe_3$) previously prepared by twin roller quenching. X-ray diffraction suggests that the structure of c-$AsTe_3$ can be described as a superstructure of elementary Te with a specific distribution of As and Te atoms. More specifically, it appears as an intergrowth of a Te subunit (3 atoms) and As2Te5 subunit (6 As + 15 Te atoms) separated with interlayer spaces. The optical transmittance measured on both crystalline and amorphous $AsTe_3$ indicates a maximum transmittance of 22 % over the infrared range 10–25 μm. Transport properties measurements, performed between 5 and 375 K, reveal that $AsTe_3$ behaves as a lightly doped, *p*-type semiconductor. The complex crystal structure combined with a small-grain-size microstructure of the sample yields extremely low lattice thermal conductivity values of 0.35 W m^{-1} K^{-1} near 300 K. This poor ability to conduct heat is the main property that gives rise to an estimated dimensionless thermoelectric figure of merit *ZT* of ~0.3 at 375 K. These findings show that the recrystallization of amorphous phases by SPS provides an effective approach for stabilizing novel phases with interesting functional properties.

1. Introduction

Thermoelectric materials, which can convert heat into electricity and vice versa, constitute an appealing alternative technology for waste-heat harvesting. The thermoelectric performance of a material is evaluated by the dimensionless thermoelectric figure of merit $ZT = \frac{\alpha^2 T}{\rho\kappa} = PT/\kappa$ where α is the thermopower (or Seebeck coefficient), $P = \alpha^2/\rho$ is the power factor, ρ is the electrical resistivity, κ is the total thermal conductivity and T is the absolute temperature [1,2].

A good thermoelectric material should simultaneously exhibit a large thermopower, a low total thermal conductivity and a low electrical resistivity. However, the mutual interdependence of these three transport properties via the carrier concentration makes the design of highly-efficient thermoelectric materials a complex task. In most state-of-the-art thermoelectric compounds, high power factors are obtained when the carrier concentration is in the range 10^{18}-10^{21} cm^{-3} at 300 K *i.e.* in heavily-doped crystalline semiconductors or semimetals [1–4]. Another ingredient paramount to achieving high *ZT* values is the combination of a complex crystalline structure and a designed microstructure to limit the contribution of the heat-carrying acoustic modes in the thermal transport [5]. A different strategy consists in focusing on materials exhibiting intrinsically very low thermal conductivity values resulting from the presence of low-energy optical modes usually observed in materials with a crystal structure containing cages or tunnels where loosely-bounded cations can reside [6–12]. Recently, breakthroughs in thermoelectric performance have been achieved in representative

* Corresponding author.
E-mail address: gaelle.delaizir@unilim.fr (G. Delaizir).

https://doi.org/10.1016/j.jallcom.2024.175918
Received 3 April 2024; Received in revised form 18 July 2024; Accepted 7 August 2024
Available online 13 August 2024

thermoelectric systems such as PbTe [4,13,14], PbSe [15–17], SnSe [18–21] and Bi_2Te_3 [22–24].

The monoclinic α-As_2Te_3 (space group $C2/m$) and its rhombohedral metastable polymorph β-As_2Te_3 (space group $R\bar{3}m$) have been recently investigated for their interesting thermoelectric properties [25–32]. Both compounds are narrow-band gap semiconductors with lattice thermal conductivity values as low as 0.8 W m^{-1} K^{-1} above 300 K. This favorable combination of transport properties led to promising thermoelectric performance upon optimization of the carrier concentration with peak ZT values as high as 0.65 at 423 K and 0.85 at 523 K in Sn-substituted β-As_2Te_3 and α-As_2Te_3, respectively [25,26]. These high values show that binary compounds in the As-Te phase diagram may be worthy of further investigations.

In this system, monoclinic α-As_2Te_3 (space group $C2/m$, no. 12) and cubic AsTe (space group $Fm\bar{3}m$, no. 225) are the only stable crystalline phases that have been reported to date [33,34]. Here, we report on the characterizations of a new metastable crystalline binary phase with the chemical composition $AsTe_3$. This compound is located near the eutectic region of the phase diagram. This phase was first stabilized in a glass composition $Cu_{15}As_{20}Te_{65}$ after a thermal treatment near the crystallization temperature, T_c, but was not further characterized [35]. Some attempts to get this compound as single phase were undertaken and finally pure $AsTe_3$ was obtained by full and congruent crystallization from the parent glass of the same composition synthesized by twin-roller, ultrafast-quenching techniques. The structure of amorphous $AsTe_3$ has been already investigated and described on the basis of X-ray diffraction, first-principles molecular dynamics (FPMD), and machine learning interatomic potentials (ML-GAP) [36] but the structure of crystalline $AsTe_3$ remains unsolved.

Glass crystallization is a powerful, non-conventional elaboration process that allows to stabilize metastable crystalline phases [37]. The thermo-mechanical cycle applied during the spark plasma sintering (SPS) treatment enabled the consolidation of the amorphous powders into either dense amorphous or crystalline samples of $AsTe_3$ depending on the dwell time applied. Because chalcogenide glasses, and especially Te-based compositions, are very attractive optical materials in the infrared range for thermal cameras or optical sensors, the optical properties of both amorphous and crystalline $AsTe_3$ have also been investigated [38].

In the present paper, we report on a thorough experimental study regarding the physical properties of this new compound and their relationship with $AsTe_3$ crystal structure with a and particular focus on the transport properties.

2. Experimental section

2.1. Synthesis

$AsTe_3$ was synthesized from As (Goodfellow, 99.99 %) and Te ingots (5 N+, 99.99 %) that were inserted a silica ampoule pumped under secondary vacuum (10^{-5} mbar). The sealed tube was subsequently heated in a rocking furnace at 1123 K for 2 h and quenched in water. The resulting bulk was crushed into small pieces, melted again before being quenched using the twin roller technique. The pieces of material were then introduced in an Argon atmosphere glove box equipped with a set-up made of a quartz tube pierced at the end and a RF induction furnace. An Ar pressure gas jet was introduced in the tube forcing the melt to flow through the hole between the rotating twin rollers. Vitreous $AsTe_3$ quenched flakes were then finally obtained [39].

The consolidation of the $AsTe_3$ amorphous powders was achieved by spark plasma sintering (SPS) using a Dr.Sinter 825 Syntex machine. The powder was introduced in a graphite die and was consolidated under vacuum (5.10^{-2} mbar) at 393 K under 50 MPa either for 2 min or 30 min to get amorphous or fully crystalline bulk samples, respectively. During the SPS process, the temperature was monitored by a thermocouple positioned through the die in the vicinity of the sample.

2.2. Sample characterizations

Powder X-ray diffraction (PXRD) data and high-temperature X-ray diffraction (HT-XRD) were collected using a Bruker D8 Advance diffractometer with reflection mode (Cu $K\alpha_1$ radiation).

Raman spectra were recorded using an In Via Reflex Renishaw micro-Raman spectrometer at 785 nm. A grating of 1200 gr/mm has been used with an objective x50LWD and using a laser power of 0.02 mW to avoid any damage of the sample.

Neutron thermodiffraction experiments were performed using the D1B powder diffraction instrument at the Institut Laue-Langevin (Grenoble, France). The instrument is a two-axis diffractometer having a banana-like Position Sensitive Detector composed by ^{3}He/CF4 1280 cells with a step of 0.1° in 2θ. The samples were placed in non-sealed cylindrical vanadium containers with an outer diameter of 8 mm and an inner diameter of 7.6 mm, under He exchange gas. A Radial Oscillating Collimator enables to remove diffraction peaks from the aluminum tail of the cryofurnace environment. The standard ILL cryofurnace and its control system allowed performing heating ramps at a heating rate of 0.1 K.min^{-1} from room temperature up to 443 K, and then between 443 K and 473 K at 3 K.min^{-1}. The incident neutron wavelength (2.530219 Å) was selected by using a pyrolytic graphite monochromator (plane 002).

Scanning electron microscopy (SEM) was carried out using a ZEISS EVO HD15 to determine the chemical composition through energy dispersive spectroscopy (EDS-SEM) of the twin-roller-quenched flakes and to probe the microstructure of $AsTe_3$ bulk samples via observations of fracture on the cross section.

Transmission electron microscopy (TEM) was performed on a FEI Tecnai G2 F20 ST equipment cooled at 77 K to avoid possible sample damages. The powdered $AsTe_3$ was ultrasonically dispersed in ethanol and a minute fraction was deposited on a grid.

The thermal behavior of amorphous $AsTe_3$ was investigated by differential scanning calorimetry (DSC) using a Mettler DSC30 equipment. Around 10 mg of powder was placed inside sealed aluminum pans. Continuous heating experiments were performed from room temperature up to 800 K using different heating rates ranging from 5 up to 40 K.min^{-1}. The crystallization activation energy E_c was calculated using the Ozawa's method specifically designed for non-isothermal study [40]. E_c was deduced from the slope of ln υ plotted as a function of $1000/T_{p1}$, where T_{p1} is the temperature at the top of the crystallization peak, following the relation:

$$\frac{d(\ln \nu)}{d\left(\frac{1}{T_{p1}}\right)} = -\frac{E_c}{R} \quad (1)$$

where R is the gas constant.

The apparent density of the SPS bulk samples and the crystalline and amorphous $AsTe_3$ powders were determined through the Archimedean principle using a Kern balance and helium pycnometer (Micromeritics) respectively.

Optical measurements were carried out at 300 K on crystalline $AsTe_3$ powders of implementing diffuse reflectance spectroscopy with a Thermo Scientific Nicolet 6700 FTIR spectrophotometer equipped with integrated sphere. Reflectance data R were used to estimate the absorption coefficient using the Kubelka-Munk relation $F(R) = (1-R)^2/2R$. The data were plotted as $(F(R)\hbar\omega)^n$ versus $\hbar\omega$, where $\hbar\omega$ is the incoming photon energy, to estimate the optical band gap E_g. The direct ($n = 2$) extrapolation of the absorption edge to zero was considered. The infrared transmittance of both amorphous and crystalline $AsTe_3$ was measured on bulk pieces using Thermo Scientific Nicolet 6700 FTIR.

2.3. Transport properties measurements

For transport properties measurements, the densified pellet of crystalline $AsTe_3$ was cut with a diamond-wire saw into samples of appropriate shape and dimensions.

Electrical resistivity, thermopower and thermal conductivity measurements were carried out at low temperatures (5 – 300 K) using the thermal transport option of a physical property measurement system (PPMS, Quantum Design). The sample, of dimensions $1.0\times1.5\times8$ mm^3, was cut perpendicularly to the pressing direction. Four copper bars were glued onto the sample using a small amount of silver epoxy. To establish a temperature gradient, a heat sink was attached to one end of the sample to maintain it at a constant temperature while applying heat at the other end. Calibrated cernox thermometers were screwed onto two copper bars glued between 2.5 and 3.5 mm apart. The temperature difference was monitored to amount to 2 % of the temperature at which the measurement was done. The voltage and temperature differences were measured at the same position along the sample. The collected data were corrected for thermal radiations by a model implemented in the TTO option software by Quantum Design that uses an accurate estimate of the bath temperature around the sample.

The electrical resistivity and thermopower were measured simultaneously from 300 up to 375 K using a ZEM-3 (ULVAC-RIKO) system on the same sample. The thermal conductivity was determined via thermal diffusivity measurements carried out between 300 and 375 K under argon atmosphere on a cylinder-shaped sample cut parallel to the pressing direction using a LFA 427 (Netzsch) equipment. Both properties are related by the formula $\kappa = dC_p\alpha_V$ where d is the thermal diffusivity, C_p is the specific heat and α_V is the experimental density. Specific heat measurements were performed by the continuous scanning method under argon atmosphere using a DSC 403 F3 equipment (Netzsch). Density was determined from geometrical dimensions and weight and its temperature dependence has been neglected in the present case. The experimental uncertainties in κ, α and ρ are estimated to be 10, 5 and 5 %, respectively, giving rise to an overall uncertainty of 17 % in the ZT values [41].

3. Results and discussion

3.1. Thermal properties, crystal structure and microstructure of crystalline $AsTe_3$

The chemical composition of different amorphous flakes and zones after twin roller quenching and after SPS was checked by SEM-EDS in order to obtain information on the chemical homogeneity. As shown in Table 1, the results were quite reproducible regardless of the chosen area. The mean atomic percentages were 75.7 ± 1.0 at% Te, 24.3 ± 1.0 at% As and 75.5 ± 1.0 % Te, 24.5 ± 1.0 % As for the amorphous flakes and the SPS bulk sample, respectively (see Table 1). Both compositions are in good agreement with the initial stoichiometric composition $AsTe_3$ and with the fact that this compound, never before obtained in a pure form and yet-to-characterize, crystallizes in a full and congruent manner from the parent glass.

The density of amorphous and crystalline $AsTe_3$ powders was found to be 5.639 ± 0.002 and 6.204 ± 0.002 g.cm^{-3}, respectively. The former value is close to that reported by Cornet *et al.* who first reported amorphous $AsTe_3$ in 1973 [42]. The $AsTe_3$ amorphous powder was then sintered by SPS under vacuum at 393 K and 50 MPa for 30 min. The geometrical density of crystalline SPS pellet is 5.97 g.cm^{-3} leading to a compactness of 96 %.

Table 1
Chemical composition of amorphous flakes and $AsTe_3$ crystalline SPS sample (standard deviation ± 1 at%).

Amorphous $AsTe_3$ flakes (twin-roller)	Zone 1	Zone 2	Zone 3
% As (at)	24.3 ±1	24 ±1	24.6 ±1
% Te (at)	75.7 ±1	76 ±1	75.4 ±1
Crystalline $AsTe_3$ (SPS)	Zone 1	Zone 2	Zone 3
% As (at)	24.8 ±1	24.4 ±1	24.1 ±1
% Te (at)	75.2 ±1	75.6 ±1	75.9 ±1

Fig. 1a shows the DSC thermograms recorded for the $AsTe_3$ amorphous composition with varying the heating rate between 5 K min^{-1} and 40 K min^{-1}. From the data collected with a heating rate of 5 K min^{-1}, a glass transition temperature T_g and a temperature of the onset of crystallization T_c of 365 K and 405 K, respectively, were inferred. The activation energy E_c determined from the Ozawa's equation corresponding to the crystallization of $AsTe_3$ is about 180 kJ mol^{-1} (Fig. 1b) which is consistent with values reported for telluride glasses. Activation energy (E_c) is one of the important parameters describing the transformation kinetics during crystallization. E_c values are found to be larger at higher crystallization temperatures.

Fig. 2a shows the PXRD patterns measured on the flakes synthesized by the twin-roller ultrafast quenching and those measured on the SPS samples. As expected, the twin-rolled flakes are amorphous. On the contrary, the SPS sample shows diffraction peaks which correspond to the crystallization of the novel $AsTe_3$ phase.

The thermodiffractogram recorded on the initial amorphous composition $AsTe_3$ quenched from 923 K allows to determine the first steps of the crystallization process between room temperature and 443 K, by steps of 5/10 K at a heating rate of 10 K/min. In good agreement with DSC data, the crystallization begins at 403 K with the formation of $AsTe_3$ as predominant phase with concomitant presence of Te (JCPDS 36–1452) and β-As_2Te_3 (JCPDS 39-1043) phases (Fig. 2b). It is noteworthy that these two impurities were already present in the parent glass and could be explained by a lower quenching rate during the twin roller process. However, the intensity of these impurities does not evolve as the temperature increases and c-$AsTe_3$ remains the major phase.

Fig. 3 shows a 3D plot of the crystallization of amorphous $AsTe_3$ as observed by neutron diffraction between 375 K and 381 K with a heating rate of 0.1 K/min. From 300 up to 376 K (not shown here), no discernible changes were observed indicating that $AsTe_3$ remained amorphous. This temperature marks the crystallization onset with three peaks appearing at 2θ values of 48.1°, 63.4° and 75.2° and corresponding to the most intense reflections of the $AsTe_3$ PXRD pattern. This temperature of first crystallization differs from the one observed by DSC and this could be explained by both the temperature measurement localization and the heating rate that are different. At about 380 K, the background suddenly flattens due to the complete crystallization of the glass, with at least three new intense peaks discernable at 45.8°, 49.2° and 94.3° (see inset of Fig. 3). Beyond this temperature, no further evolution with increasing temperature up to 473 K occurs.

The PXRD pattern of sintered $AsTe_3$ (Fig. 2) shows 9 relatively intense main peaks in the 10–80° (2θ) range, in addition to many low-intensity peaks with varying widths. These 9 peaks could be easily indexed with a hexagonal unit cell of parameters a = b = 4.1270 Å and c = 6.1468 Å. Interestingly, these values were found to be relatively close to the unit cell parameters of elemental Te (a = b = 4.456 Å and c = 5.921 Å), which crystallizes in the trigonal $P3_121$ space group with Te atoms in the 3a Wyckoff positions. In addition, the structure of elemental Te modified using the as-obtained cell parameters was able to reproduce well the 9 main peaks both in positions and intensities and led to an atomic density of ρ = 0.0331 at/Å^3, which is very close to the experimental value obtained for c-$AsTe_3$ (ρ = 0.0326 at/Å^3). These results suggested that the crystal structure of c-$AsTe_3$ could be described as a superstructure of elementary Te with a specific distribution of As and Te atoms in the crystallographic sites of the parent structure.

Unfortunately, it was not possible to go much further with conventional methods of structure determination. Full indexation of the PXRD diagram was not successful, nor were crystal growth experiments to obtain $AsTe_3$ single crystals and transmission electron microscopy

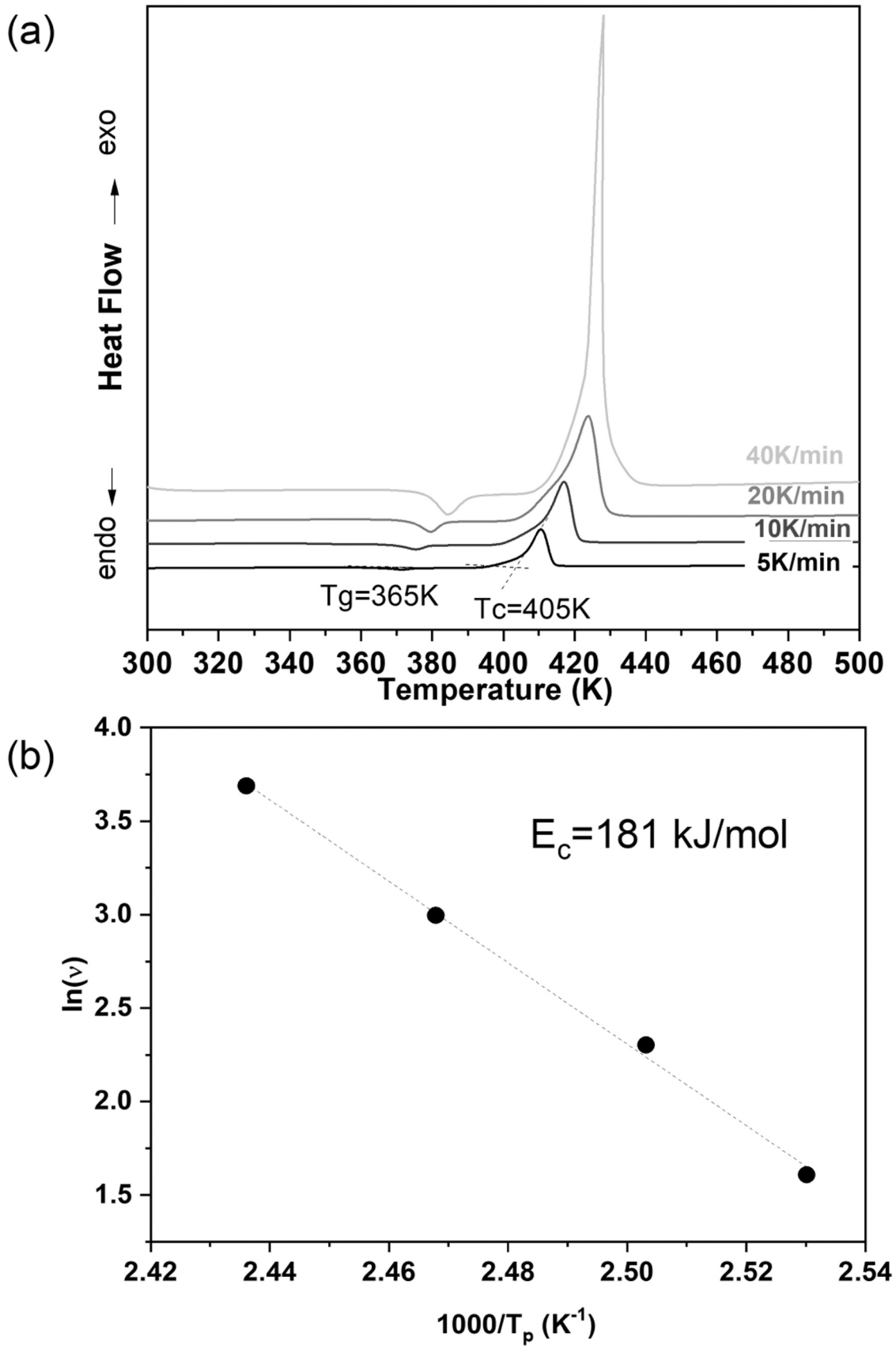

Fig. 1. (a) DSC thermograms of $AsTe_3$ amorphous powder (obtained after twin-roller quenching) at different heating rates (from 5 K/min to 40 K/min), (b) Plot of ln ν as a function of $1000/T_p$ allowing the calculation of the $AsTe_3$ crystallization energy E_c using Ozawa's method.

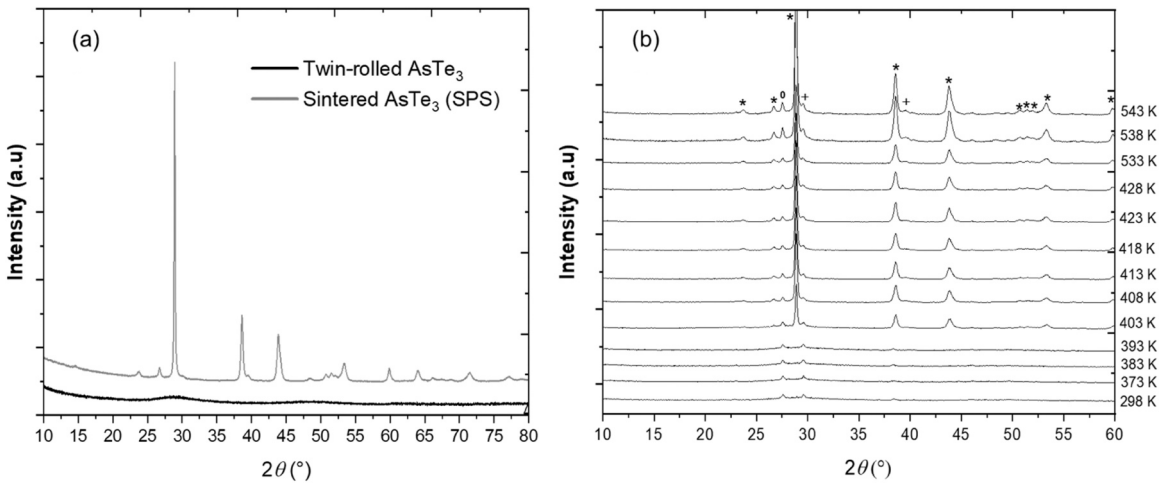

Fig. 2. (a) PXRD patterns of powder after twin-roller quenching (black curve) and powder sintered at 120°C for 30 min (50 MPa) by SPS (red curve), (b) HT-XRD of $AsTe_3$ amorphous powder (* unreported $AsTe_3$, 0 Te (JCPDS 36–1452) and + β-As_2Te_3, (JCPDS 39–1043)).

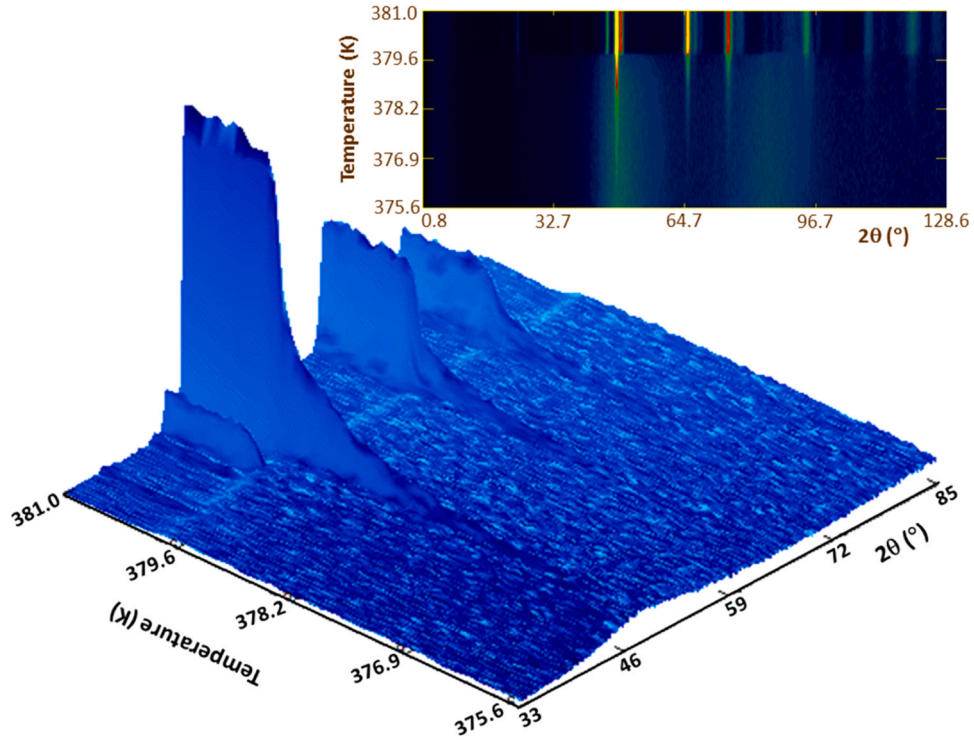

Fig. 3. 3D plots of the neutron thermodiffraction data (λ=2.530219 Å) collected between 33° and 85° as a function of temperature for the $AsTe_3$ amorphous sample. The inset shows a 2D mapping of the diffraction data between 0.8° and 128.6°.

observations at 77 K. For this reason, we resorted to an unconventional approach combining PXRD, semi-automated atomic scale modeling and experimental atomic pair distribution function (PDF) analysis to propose a realistic structural model of c-$AsTe_3$ that highlights the structural complexity and local order of this phase. The details of this study is beyond the scope of the present manuscript and have been submitted elsewhere [43]. For discussion purposes, we describe below the proposed model in this investigation. It is important to keep in mind that, while providing a description in good overall agreement with experimental results, this model alone does not capture the entire complexity of the crystalline $AsTe_3$ phase.

The proposed model has monoclinic symmetry and is illustrated in Fig. 4a. It appears as an intergrowth of a Te subunit (3 Te atoms, highlighted in pale red in Fig. 4a) and an As_2Te_5 subunit (6 As + 15 Te atoms) separated with interlayer spaces consistent with van der Waals interactions. The latter contains local structural features (highlighted in grey in Fig. 4a) similar to those found in α-As_2Te_3 (shown in Fig. 4b), albeit with substitutions of As atoms by Te atoms (highlighted in black in Fig. 4b and 4c) on both sides of the intergrown Te subunit. As a result of these As/Te substitutions, the unit cell of the $AsTe_3$ model structure is found to contain two domains of distinct compositions: a pure-Te composition domain almost 1 nm in thickness (9 Te atoms) with local structural arrangements visually similar to those found in elemental-Te (Fig. 4b) and a mixed-composition domain consisting of 6 As and 9 Te atoms (As_2Te_3). As illustrated in Fig. 4c, it translates at the atomic scale into a diversity of Te and As coordination states, albeit all in more or less distorted octahedral environments (considering a cutoff of 3.3 Å) with various combinations of Te and/or As bonded and/or non-bonded

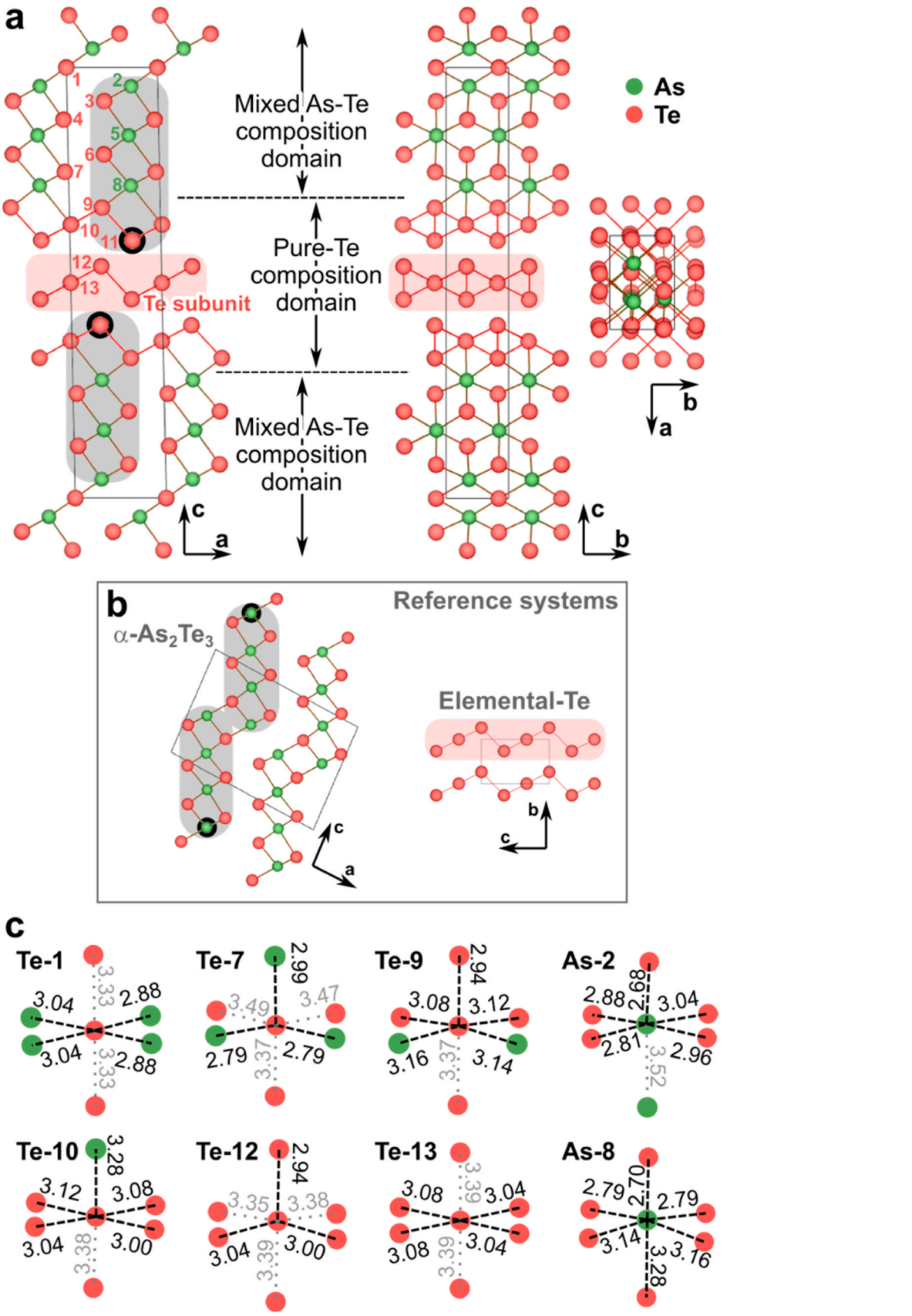

Fig. 4. (a) The best candidate structure model proposed in [43] for c-$AsTe_3$ viewed along all three crystallographic axes. (b) Crystal structures of known α-As_2Te_3 and elemental-Te shown for comparison purposes. (c) Representative local environments identified with As-Te and Te-Te cutoff distances of 3.5 Å. Atomic proximities are shown as dashed black lines below a cutoff of 3.3 Å, which corresponds to a minimum in both As-Te and Te-Te partial radial distribution functions (not shown), and as dotted gray lines above this value.

neighbors. These results are in good agreement with the recent work of An *et al.* who suggested that As-doped tellurium (as well as Bi or Sb dopants) samples feature a dual-phase structure consisting of a nearly undoped Te matrix as well as As_2Te_3 (respectively Bi_2Te_3 and Sb_2Te_3) precipitates that are responsible for improved thermoelectric properties [44].

The synthesis process (crystallization of the parent glass) and the far-from-perfect crystallinity of the sample suggest that disorder of various possible origins can be present in the structure, even though the sudden plateau observed in variable-temperature neutron diffraction data (Fig. 3) indicates a complete crystallization of the material.

To support the structure model proposed in [43] for c-$AsTe_3$, we compare below the Raman spectra of c-$AsTe_3$ with those recorded on elemental Te, β-As_2Te_3 and α-As_2Te_3 (Fig. 5a). Each spectrum was decomposed, as shown in Fig. 5b-5e, in an attempt to reveal and locate potentially-overlapping contributions. In As-Te crystalline compounds, the modes with frequencies higher than 160 cm^{-1} are dominated by light As atoms, modes with frequencies between 100 and 150 cm^{-1} are defined by the vibration of heavy Te atoms and modes with frequencies below 100 cm^{-1} are collective or lattice modes of vibration where groups of As and/or Te atoms move in or out of phase [45]. It must be stressed that Raman spectra of α-As_2Te_3 (layered structure with monoclinic C2/m symmetry) and β-As_2Te_3 (rhombohedral structure with $R\bar{3}m$ symmetry) resemble that of elemental Te, which crystallizes in a trigonal space group since they both exhibit the three active Raman phonon modes characteristics of Te but with various intensities and shifts in frequencies. Further details about the Raman peak positions corresponding to vibrational modes in α and β-As_2Te_3 phases, and their corresponding attribution can be found in Refs. [45,46]. The most intense Raman peak of elemental Te located at ~122 cm^{-1} is related to the A1 mode, corresponding to atoms moving in the basal plane (*i.e.* perpendicular to the c-axis) (see Fig. 5e). Two degenerate E modes also exist in Te, which split into predominately bond-bending and bond-stretching types. The E1 mode at ~94 cm^{-1} is caused by rotation around the *a*-axis, and the E2 mode at 142 cm^{-1} is assigned to asymmetric stretching mainly along the *c*-axis [47,48]. It is noteworthy that some Te-related modes (especially the A1 and E2 modes) can be indexed as impurities in both α and β-As_2Te_3 phases (see black thick decomposed curves in Fig. 5b and 5c). V. Cuenca-Gotor *et al.* and R. Vilaplana *et al.* explained the presence of these unexpected crystalline Te modes by the effect of laser irradiation during the Raman experiments that may induce local heating even using a low power laser since no crystalline Te can be indexed in both α and β-As_2Te_3 XRD patterns [45,46] (see Fig. 5b, 5c). Surprisingly the E1 mode related to crystalline Te is not found in our α and β-As_2Te_3 Raman spectra suggesting that further investigations for a better understanding of the presence of these modes may be undertaken.

The decomposition of c-$AsTe_3$ Raman spectrum reveals five bands. Three of them (at 94, 122 and 137 cm^{-1}) match perfectly the Te Raman spectrum (in contrast to the peaks of unknown origin previously attributed to impurities in α- and β-As_2Te_3) and may correspond to the intergrown pure-Te sub-units depicted in the $AsTe_3$ crystalline structural model obtained from first-principles modeling. The two others modes observed at 169 cm^{-1} and 191 cm^{-1} may be assigned to the sub-unit

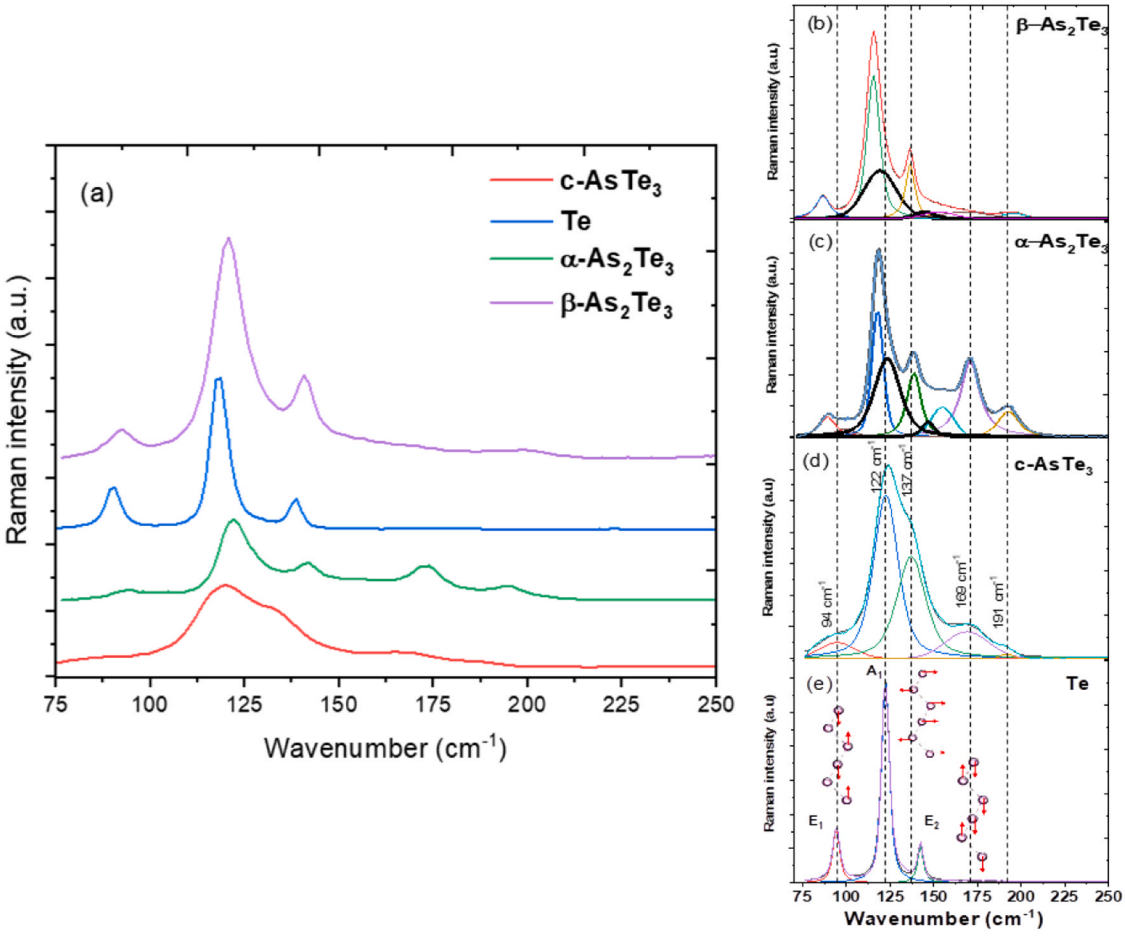

Fig. 5. (a) Raman spectra of crystalline (c-$AsTe_3$) $AsTe_3$, elemental Te, α-As_2Te_3 and β-As_2Te_3, Decomposition of Raman spectra (b) β-As_2Te_3, (c) α-As_2Te_3, (d) c-$AsTe_3$ and (e) Te spectra and its corresponding atom vibration directions. (Dashed lines serve as eye guide and thick black decomposed curves in (b) and (c) correspond to crystalline Te as impurity according to [45] and [46]).

As_2Te_5 domains linked to the mode A_g in the *ac* plane also present in α-As_2Te_3 [46]. The Raman spectrum of c-$AsTe_3$ is thus intermediate between those of Te and α-As_2Te_3, in agreement with the local structural similarities identified from the modeling. It must also be emphasized that the Raman spectrum of c-$AsTe_3$ is significantly broader than those of crystalline As_2Te_3 and Te. This indicates the presence of a positional disorder in the structure, affecting both bond lengths and angles, the cause of which is not yet well established, but which could be related to an underlying As/Te chemical disorder.

Finally, the microstructure observed on a SPS fresh fractured crystalline sample reveals some residual porosity as shown in Fig. 6a and 6b. SEM observations show some nano-grains with size less than 50 nm. The microstructure of $AsTe_3$ was further probed at the atomic scale by TEM observations performed on a thin section of an $AsTe_3$ SPS sample. The size of the different monocrystalline domains does not exceed few tens of nm (Fig. 6c and 6d).

3.2. Transport properties

In light of the interesting thermoelectric properties already demonstrated in α and β-As_2Te_3, the transport properties of c-$AsTe_3$ were studied. Fig. 7a shows the temperature dependence of the electrical resistivity ρ. Upon heating, ρ rapidly decreases by five orders of magnitude, from around 10^7 μΩ.m at 5 K to 150 μΩ.m at 375 K, indicating that $AsTe_3$ behaves as a semiconductor. The room-temperature ρ value is close to that of lightly-doped elemental Te from which the crystal structure of $AsTe_3$ derives [5]. The $\rho(T)$ data were further analyzed by an activation model according to the relation $\ln\rho = \frac{E_g}{2k_BT} + A$ where k_B is the Boltzmann constant and A is a constant. A linear fit to the $\ln\rho$ versus $1/T$ data in the 300 – 375 K temperature range yields an estimated band gap E_g of 0.32 eV, in reasonable agreement with the optical band gap of 0.43 eV determined by absorption spectroscopy (see below). This small difference may be attributed to the narrow temperature range over which the $\rho(T)$ data were fitted, with the activation model not being applicable at lower temperatures. Below 300 K, the data were rather analyzed using the variable-range-hopping (VRH) model $\rho(T) = \rho_0 e^{\left(\frac{T_0}{T}\right)^n}$, characteristic of an impurity hopping conduction typically observed in semiconductors in which a large number of impurity states form a narrow band. In this equation, ρ_0 and T_0 are constants and the exponent n can be written as $n = 1/(d+1)$ where d is the dimension of the conduction mechanism. This equation describes well the experimental data between 300 K down to about 30 K with n = ¼ suggesting that the electrical conduction is mostly three-dimensional ($d = 3$) (see inset in Fig. 7a). The lack of further decrease in ρ at high temperatures indicates the absence of minority carrier effects due to the moderate temperature range over which $AsTe_3$ is stable as shown by HT-XRD (Fig. 2b).

The temperature dependence of the thermopower α is shown in Fig. 7b. As in α- and β-As_2Te_3, the α values are positive in the whole temperature range indicating that holes are the dominant charge carriers in $AsTe_3$. The $\alpha(T)$ dependence confirms the semiconducting nature of crystalline $AsTe_3$, with a non-linear variation with temperature below 50 K usually observed in lightly-doped semiconductors. Above this temperature, α increases monotonically with increasing temperature to reach 185 μV K^{-1} at 375 K.

The temperature dependence of the specific heat C_p is shown in Fig. 8a. Near 300 K, the C_p values approach the Dulong-Petit limit $3NR$ where N is the number of atoms per formula unit and R is the ideal gas constant. The low-temperature C_p/T data obeys the conventional free-electron formula $\frac{C_p}{T} = \gamma + \beta T^2$ where γ is the Sommerfeld coefficient reflecting the electronic contribution and β is a parameter related to the lattice contribution.

The best fit to the data below 3.5 K yields a γ value indistinguishable from zero to within experimental uncertainty corresponding to a null density of states of the Fermi level, consistent with the semiconducting nature of $AsTe_3$. The parameter β corresponds to a Debye temperature $\theta_D = \left(\frac{12\pi^4 NR}{5\beta}\right)^{1/3}$ of 154 K. Plotting the phonon contribution to the specific heat C_{ph}/T^3 as a function of T (Fig. 8b) shows a pronounced maximum centered near 10 K that reflects an excess of vibrational density of states over the Debye term. Insights into the phonon spectrum can be usually obtained by fitting these data using a combination of

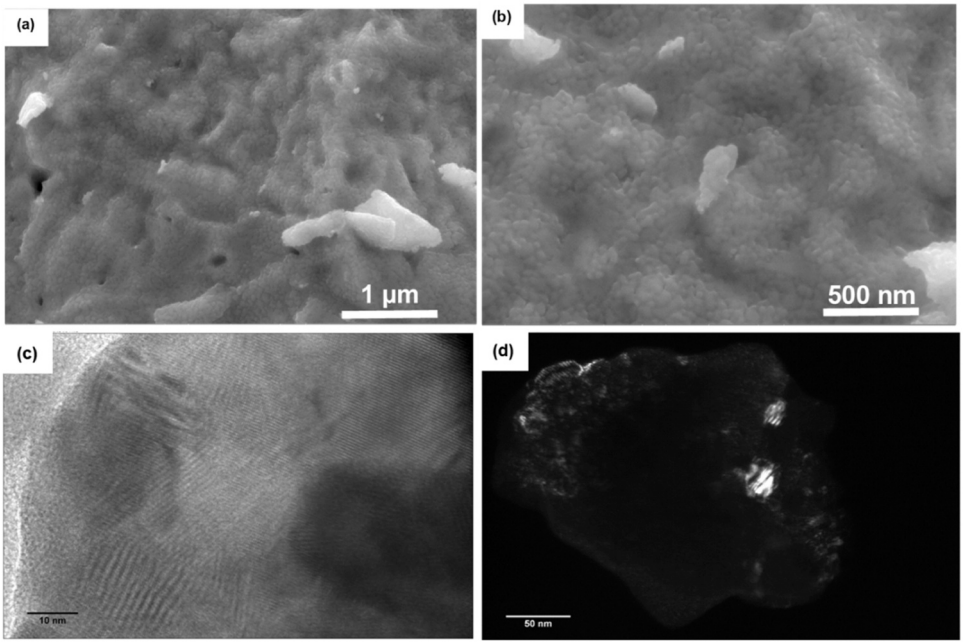

Fig. 6. SEM images of a fresh fracture of crystalline $AsTe_3$ (SPS sample sintered at 393 K for 30 min under 50 MPa), (a) low magnification, (b) high magnification. TEM observations of $AsTe_3$ crystalline SPS sample: (c) bright field, (d) dark field.

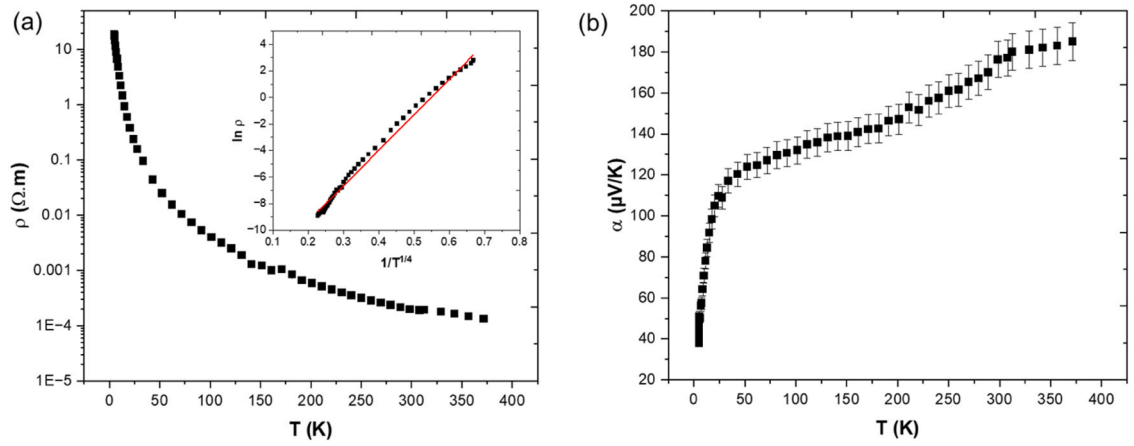

Fig. 7. (a) Electrical resistivity and (b) Seebeck coefficient of polycrystalline $AsTe_3$ as a function of temperature. The inset of figure (a) shows the lnρ versus $T^{-1/4}$ according to the variable-range-hopping (VRH) model.

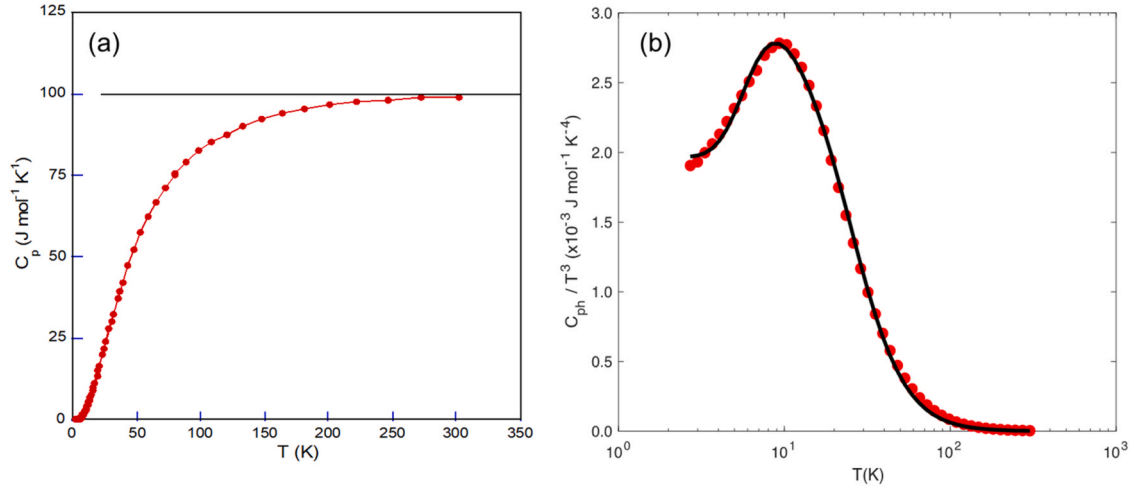

Fig. 8. (a) Specific heat C_p as a function of temperature of $AsTe_3$. The horizontal solid black line stands for the Dulong-Petit limit of 3NR. (b) C_{ph}/T^3plotted as a function of T (C_{ph} is the phonon contribution to the specific heat C_p). The solid black curve corresponds to the best fit to the data according to Eq.(1).

Einstein and Debye terms. This approach has been widely used in cage-like compounds such as skutterudites or clathrates for which the large thermal vibrations of the encaged ions are associated with low-energy optical phonon modes, which can be adequately described by Einstein-like contributions. In this context, the low-temperature $C_p(T)$ data are then modelled by a combination of Debye and Einstein terms through the relation

$$C_p = C_D + C_{Ei} = 9N_D R\left(\frac{T}{\theta_D}\right)^3 \int_0^{\theta_D/T} \frac{x^4 e^x}{(e^x-1)^2}dx + \sum_i p_i N_{Ei} R\left(\frac{\theta_{Ei}}{T}\right)^2 \frac{e^{\theta_{Ei}/T}}{(e^{\theta_{Ei}/T}-1)^2} \quad (1)$$

where C_D is the lattice contribution described within the Debye model, C_{Ei} is the Einstein contribution of the i^{th} vibrational mode of the guest atoms, $x = \hbar\omega/k_B T$ with $\hbar$ the reduced Planck constant and k_B the Boltzmann constant, N_D is the number of Debye oscillators per formula unit and p_i, N_{Ei} and θ_{Ei} are the degrees of freedom, the number of Einstein oscillators, and the Einstein temperature related to the i^{th} vibrational mode, respectively. The best fit to the data (Fig. 8b), with the two Einstein temperatures and the spectral weights allowed to vary, shows that this model captures reasonably well the temperature dependence of the C_p data, yielding an effective Debye temperature θ_D of 134 K, and Einstein temperatures θ_{E1} = 44.1 K and θ_{E2} = 172.8 K. The θ_{E1} value corresponds to a low-energy optical mode at 3.8 meV (0.93 THz). This value is similar to those determined in α-As_2Te_3 (around 0.6 THz, that is, 2.5 meV) and β-As_2Te_3 (around 0.8 THz, that is, 3.3 meV) by lattice dynamics calculations and Raman spectroscopy [7,8]. The presence of these low-energy optical modes strongly limits the energy window over which the acoustic branches disperse, thereby lowering the lattice thermal conductivity.

In agreement with these considerations, $AsTe_3$ exhibits extremely low thermal conductivity values κ of around 0.35 W m^{-1} K^{-1} in the whole temperature range (Fig. 9), similar to those reported for α- and β-As_2Te_3. Due to the rather high ρ values, the measured κ values nearly entirely reflect the lattice contribution κ_L according to the Wiedemann-Franz law $\kappa_e = LT/\rho$ that relates the electronic contribution κ_e to ρ via the Lorenz number L. The very low κ_L values and the absence of an Umklapp peak indicate that the thermal transport in $AsTe_3$ mirrors that observed in amorphous compounds. The κ_L values approach the glassy limit, according to the model of Cahill and Pohl, estimated to be equal to 0.33 W m^{-1} K^{-1} from the longitudinal (v_L = 2967 m s^{-1}) and transverse (v_T = 1422 m s^{-1}) sound velocities measured at 300 K by a pulse-echo method. The significant consequences on phonon-phonon scattering processes implied by the presence of low-energy optical modes explains both the very low κ_L values of $AsTe_3$ and their temperature dependence. Indeed, these modes open an additional channel of three-phonon Umklapp scattering processes, making them still active at low

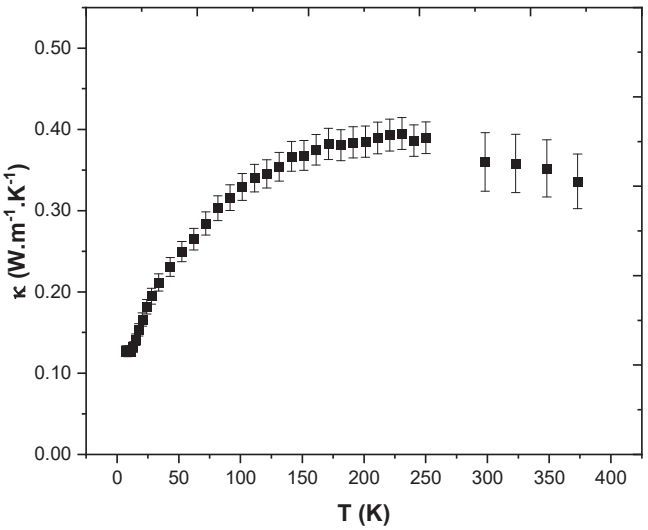

Fig. 9. Thermal conductivity of polycrystalline $AsTe_3$ as a function of temperature.

temperatures and explaining the absence of a pronounced crystalline peak. The key role played by these modes in shaping the temperature dependence of κ_L has been demonstrated in several low-κ_L compounds such as tetrahedrites, InTe or type-I clathrates [49–52]. Furthermore, the presence of nano-crystallites with an average grain size of 50 nm observed by SEM and TEM in these polycrystalline $AsTe_3$ specimens also contributes to lower the κ_L values through enhanced grain boundary and point-defect scattering that predominantly scatter low-energy and high-energy phonons, respectively. Both mechanisms are thus expected to concomitantly reduce the κ_L values and weakens their temperature dependence [53].

Fig. 10 shows the temperature dependence of the dimensionless thermoelectric figure of merit *ZT*. A peak *ZT* value of 0.28 is achieved in $AsTe_3$ at 375 K, a value higher than those measured in pristine α- and β-As_2Te_3 at the same temperature. We note that these *ZT* values should be taken with some caution due to the anisotropic crystal structure of $AsTe_3$ that may lead to some degree of anisotropy in the transport properties, as observed in both α- and β-As_2Te_3. Thus, the combination of transport properties measured parallel and perpendicular to the

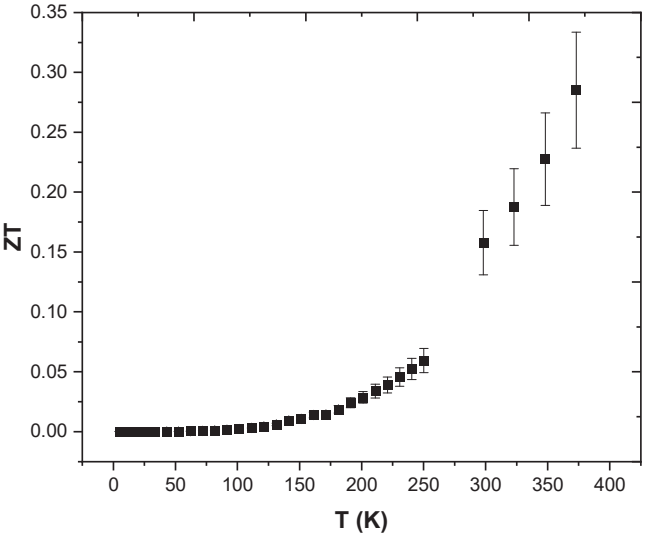

Fig. 10. Dimensionless thermoelectric figure of merit ZT of polycrystalline $AsTe_3$ as a function of temperature. The error bars represent the uncertainties (17 %).

pressing direction likely results in overestimated *ZT* values. Nevertheless, the comparison between the room-temperature κ values of the low and high-temperature data sets are close, suggesting that the possible anisotropy between the parallel and perpendicular directions should be small. Thus, although possibly overestimated, the present *ZT* values are expected to provide a reasonable estimation of the actual *ZT* values of $AsTe_3$.

3.3. Optical measurements

Fig. 11 shows the optical absorption spectra collected on both amorphous and crystalline $AsTe_3$ compounds assuming direct transitions. The spectrum of crystalline $AsTe_3$ shows an increase up to around 0.4 eV where a steep rise is observed and that likely corresponds to the optical band gap E_g with an estimated value of 0.43 eV. This value is close to those determined from similar optical data for α-As_2Te_3 (0.43 eV) and β-As_2Te_3 (0.30 eV) [25,26]. The spectrum of amorphous $AsTe_3$ exhibits a different behavior with a band gap of around 0.70 eV which is in good agreement with the band gap observed in transmittance experiments at ~ 2 μm (Fig. 8b).

The measurements of the optical transmittance of the $AsTe_3$ SPS glass and corresponding crystalline bulk samples (Fig. 8b) show that glass $AsTe_3$ exhibits a transmittance of up to 22 % in the range 10–25 μm. The absorption band around 12 μm is attributed to As-O bonds of impurities. While the corresponding crystalline $AsTe_3$ compound exhibits a nanostructure with grains less than 50 nm, its transmittance is zero in the range 2–25 μm. This result could be explained by the numerous micropores observed on SEM images (see Fig. 6a) that induces light scattering, especially in the visible range. Moreover, the difference in densities between the $AsTe_3$ glass and its crystalline counterpart is high (almost 9 %). Thus, the crystallization induces mechanical strain resulting in micro-cracks that can act as scattering centers.

4. Conclusion

We reported on a detailed investigation of the synthesis, crystal structure, thermal, optical and transport properties of the novel binary $AsTe_3$ compound. Bulk crystalline samples of $AsTe_3$ have been successfully synthesized from the full and congruent crystallization of the parent glass by spark plasma sintering. X-ray diffraction and X-ray total scattering coupled with atomic scale modeling methods suggest that the crystal structure of $AsTe_3$ derives from the structure of elemental Te with suspected intergrowth of pure Te sheets and α-As_2Te_3-like domains. Optical properties of $AsTe_3$ glass are promising as a transmittance of 22 % up to 25 μm was recorded with no prior element purification and optimization of the SPS thermomechanical cycle. The small grain size (~60 nm) evidenced in the crystalline $AsTe_3$ compound should also favor good optical properties and garner some interest in this field. Transport properties measurements combined with absorption spectroscopy revealed that $AsTe_3$ is a narrow-band-gap semiconductor and a poor thermal conductor, as its cousin compounds α- and β-As_2Te_3. Despite being undoped, the beneficial combination of relatively low electrical resistivity and thermal conductivity and high thermopower results in a promising peak *ZT* value of 0.3 at 375 K. Further investigations would be worthwhile to determine whether the synthesis method used herein allows for a further optimization of the thermoelectric properties by extrinsic doping. On a more general aspect, these results show that using the thermomechanical SPS process to crystallize amorphous phases can lead to the discovery of novel metastable phases with interesting functional properties.

CRediT authorship contribution statement

Vivian Nassif: Investigation. **Cédric Morin:** Formal analysis, Data curation, Conceptualization. **Sylvian Cadars:** Methodology, Formal analysis. **Jean-Baptiste Vaney:** Methodology, Investigation, Data

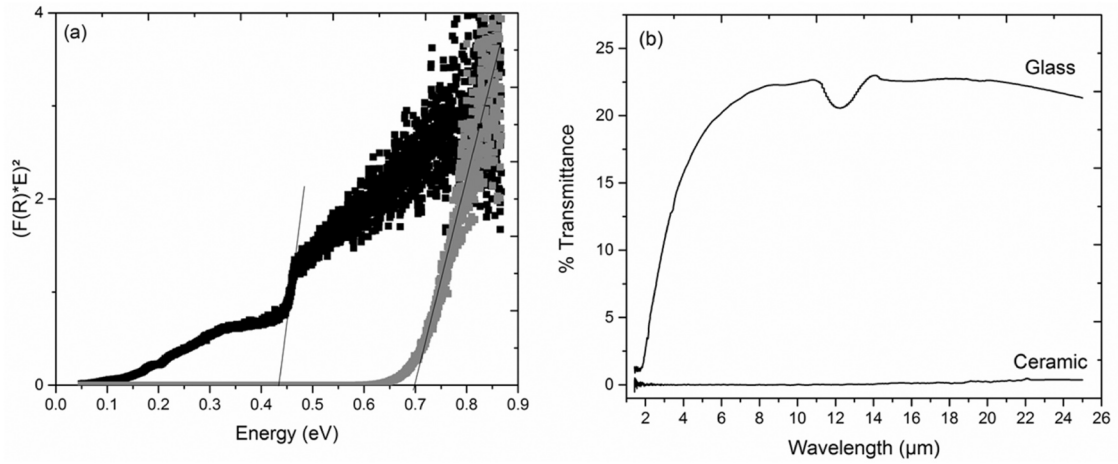

Fig. 11. (a) Optical absorption spectrum for amorphous (•) and crystalline (■) $AsTe_3$ plotted as $[F(R)\times E]^2$ vs ($E = \hbar\omega$) (that is for direct transition). The extrapolation of the solid black line to zero provides an estimate of the optical band gap E_g. (b) Transmittance in infrared range of the $AsTe_3$ glass and fully crystallized samples (thickness: 0.5 mm).

curation. **Bertrand Lenoir:** Supervision, Project administration. **Gaelle Delaizir:** Writing – original draft, Project administration, Funding acquisition. **Petr Levinsky:** Investigation. **Gabriel Cuello:** Data curation. **Mickael Bigot:** Methodology, Investigation. **Maggy Colas:** Formal analysis, Data curation. **Andrea Piarristeguy:** Resources, Methodology. **Jean-Paul Laval:** Methodology, Data curation. **Christophe Candolfi:** Resources, Methodology, Investigation. **Olivier Masson:** Formal analysis, Data curation, Conceptualization. **Julie Carreaud:** Supervision, Resources, Methodology. **Assil Bouzid:** Software, Data curation, Conceptualization. **Annie Pradel:** Supervision. **Eric Alleno:** Supervision, Methodology, Investigation, Conceptualization. **Judith Monnier:** Investigation, Formal analysis. **Julie Cornette:** Formal analysis, Data curation.

Declaration of Competing Interest

The authors declare that they have no known competing financial interests or personal relationships that could have appeared to influence the work reported in this paper.

Data availability

Data will be made available on request.

References

[1] D.M. Rowe, Thermoelectrics and its Energy Harvesting, CRC Press, Boca Raton, FL, 2012.
[2] H.J. Goldsmid, Thermoelectric Refrigeration, Springer, New York, USA, 1964.
[3] Q. Yan, M.G. Kanatzidis, High-performance thermoelectrics and challenges for practical devices, Nat. Mater. 21 (2022) 503.
[4] G. Tan, F. Shi, S. Hao, L.-D. Zhao, H. Chi, X. Zhang, C. Uher, C. Wolverton, V. P. Dravid, M.G. Kanatzidis, Non-equilibrium processing leads to record high thermoelectric figure of merit in PbTe–SrTe, Nat. Commun. 7 (2016) 12167, https://doi.org/10.1038/ncomms12167.
[5] J. Snyder, E. Toberer, Complex thermoelectric materials, Nat. Mater. 7 (2008) 105.
[6] H.A. Eivari, Z. Sohbatzadeh, P. Mele, M.H.N. Assadi, Low thermal conductivity: fundamentals and theoretical aspects in thermoelectric applications, Mater. Today Energy 21 (2021) 100744.
[7] D.J. Safarik, T. Klimczuk, A. Llobert, D.D. Byler, J.C. Lashley, J.R. O'Brien, N. R. Dilley, Localized anharmonic rattling of Al atoms in VAl10.1, Phys. Rev. B 85 (2012) 014103.
[8] M.M. Koza, A. Leithe-Jasper, E. Sischka, W. Schnelle, H. Borrmann, H. Mutka, Y. Grin, Effect of the electropositive elements A = Sc, La, and Ce on the microscopic dynamics of AV2Al20, Phys. Chem. Chem. Phys. (2014).
[9] M.M. Koza, H. Mutka, Y. Okamoto, J.-I. Yamaura, Z. Hiroi, On the microscopic dynamics of the 'Einstein solids' AlV2Al20 and GaV2Al20, and of YV2Al20: a benchmark system for 'rattling' excitations, Phys. Chem. Chem. Phys. 15 (2015) 24837.
[10] K. Suekuni, M.A. Avila, K. Umeo, T. Takabatake, Cage-size control of guest vibration and thermal conductivity in Sr8Ga16Si30−xGex, Phys. Rev. B 75 (2007) 195210.
[11] G.S. Nolas, J.L. Cohn, J.S. Dyck, C. Uher, J. Yang, Transport properties of polycrystalline type-I Sn clathrates, Phys. Rev. B 65 (2002) 165201.
[12] M.K. Jana, K. Pal, A. Warankar, P. Mandal, U.V. Waghmare, K. Biswas, Intrinsic rattler-induced low thermal conductivity in zintl type TlInTe2, J. Am. Chem. Soc. 139 (2017) 4350.
[13] Z.-Z. Luo, S. Cai, S. Hao, T.P. Bailey, Y. Luo, W. Luo, Y. Yu, C. Uher, C. Wolverton, V.P. Dravid, Z. Zou, Q. Yan, M.G. Kanatzidis, Extraordinary role of Zn in enhancing thermoelectric performance of Ga-doped n-type PbTe, Energy Environ. Sci. 15 (2022) 368–375, https://doi.org/10.1039/D1EE02986J.
[14] P. Xu, W. Zhao, X. Liu, B. Jia, J. He, L. Fu, B. Xu, Dramatic enhancement of thermoelectric performance in PbTe by unconventional grain shrinking in the sintering process, Adv. Mater. 34 (2022) 2202949, https://doi.org/10.1002/adma.202202949.
[15] B. Ge, H. Lee, J. Im, Y. Choi, S.-Y. Kim, J.Y. Lee, S.-P. Cho, Y.-E. Sung, K.-Y. Choi, C. Zhou, Z. Shi, I. Chung, Engineering an atomic-level crystal lattice and electronic band structure for an extraordinarily high average thermoelectric figure of merit in n-type PbSe, Energy Environ. Sci. 16 (2023) 3994–4008, https://doi.org/10.1039/D3EE01226C.
[16] B. Ge, H. Lee, L. Huang, C. Zhou, Z. Wei, B. Cai, S.-P. Cho, J.-F. Li, G. Qiao, X. Qin, Z. Shi, I. Chung, Atomic level defect structure engineering for unusually high average thermoelectric figure of merit in n-type PbSe rivalling PbTe, Adv. Sci. 9 (2022) 2203782, https://doi.org/10.1002/advs.202203782.
[17] L. Xu, Y. Xiao, S. Wang, B. Cui, D. Wu, X. Ding, L.-D. Zhao, Dense dislocations enable high-performance PbSe thermoelectric at low-medium temperatures, Nat. Commun. 13 (2022) 6449, https://doi.org/10.1038/s41467-022-34227-3.
[18] S. Byun, B. Ge, H. Song, S.-P. Cho, M.S. Hong, J. Im, I. Chung, Simultaneously engineering electronic and phonon band structures for high-performance n-type polycrystalline SnSe, Joule 8 (2024) 1520–1538, https://doi.org/10.1016/j.joule.2024.02.013.
[19] S. Chandra, U. Bhat, P. Dutta, A. Bhardwaj, R. Datta, K. Biswas, Modular nanostructures facilitate low thermal conductivity and ultra-high thermoelectric performance in n-type SnSe, Adv. Mater. 34 (2022) 2203725, https://doi.org/10.1002/adma.202203725.
[20] C. Zhou, Y.K. Lee, Y. Yu, S. Byun, Z.-Z. Luo, H. Lee, B. Ge, Y.-L. Lee, X. Chen, J. Y. Lee, O. Cojocaru-Mirédin, H. Chang, J. Im, S.-P. Cho, M. Wuttig, V.P. Dravid, M. G. Kanatzidis, I. Chung, Polycrystalline SnSe with a thermoelectric figure of merit greater than the single crystal, Nat. Mater. 20 (2021) 1378–1384, https://doi.org/10.1038/s41563-021-01064-6.
[21] A. Banik, K. Biswas, A game-changing strategy in SnSe thermoelectrics, Joule 3 (2019) 636–638, https://doi.org/10.1016/j.joule.2019.03.001.
[22] B. Zhu, X. Liu, Q. Wang, Y. Qiu, Z. Shu, Z. Guo, Y. Tong, J. Cui, M. Gu, J. He, Realizing record high performance in n-type Bi2Te3-based thermoelectric materials, Energy Environ. Sci. 13 (2020) 2106–2114, https://doi.org/10.1039/D0EE01349H.
[23] H. Lee, T. Kim, S.C. Son, J. Kim, D. Kim, J. Lee, I. Chung, Unique Microstructures and High Thermoelectric Performance in n–type Bi2Te2.7Se0.3 by the Dual Incorporation of Cu and Y, Mater. Today Phys. 31 (2023) 100986, https://doi.org/10.1016/j.mtphys.2023.100986.
[24] R. Deng, X. Su, Z. Zheng, W. Liu, Y. Yan, Q. Zhang, V.P. Dravid, C. Uher, M. G. Kanatzidis, X. Tang, Thermal conductivity in $Bi_{0.5}Sb_{1.5}Te_{3+x}$ and the role of dense dislocation arrays at grain boundaries, Sci. Adv. 4 (2018) eaar5606, https://doi.org/10.1126/sciadv.aar5606.
[25] J.B. Vaney, J. Carreaud, G. Delaizir, A. Piarristeguy, A. Pradel, E. Alleno, J. Monnier, E.B. Lopes, A.P. Gonçalves, A. Dauscher, C. Candolfi, B. Lenoir, High

thermoelectric performance in Sn-substituted α-As2Te3, J. Mater. Chem. C 4 (2016) 2329–2338.
[26] J.-B. Vaney, J. Carreaud, G. Delaizir, A. Pradel, A. Piarristeguy, C. Morin, E. Alleno, J. Monnier, A.P. Gonçalves, C. Candolfi, A. Dauscher, B. Lenoir, High-temperature thermoelectric properties of Sn-doped β-As2Te3, Adv. Elec. Mater. 1 (2015) 1400008.
[27] J.B. Vaney, G. Delaizir, E. Alleno, B. Wiendlocha, J. Tobola, C. Gendarme, B. Malaman, A. Dauscher, C. Candolfi, B. Lenoir, Effect of isovalent substitution on the electronic structure and thermoelectric properties of the solid solution α As2Te3–xSex (0 ≤ x ≤ 1.5), Inorg. Chem. 56 (2017) 2248–2257.
[28] J.-B. Vaney, G. Delaizir, A. Piarristeguy, J. Monnier, E. Alleno, E.B. Lopes, A. P. Goncalves, A. Pradel, A. Dauscher, C. Candolfi, B. Lenoir, High-temperature thermoelectric properties of the β-As2-xBixTe3 solid solution, APL Mater. 4 (2016) 104901.
[29] J.-B. Vaney, J. Carreaud, G. Delaizir, C. Morin, J. Monnier, E. Alleno, A. Piarristeguy, A. Pradel, A.P. Goncalves, E.B. Lopes, C. Candolfi, A. Dauscher, B. Lenoir, Thermoelectric properties of the α-As2Te3 crystalline phase, J. Electron. Mater. 45 (2016) 1447–1452.
[30] J.-B. Vaney, J. Carreaud, G. Delaizir, C. Morin, J. Monnier, E. Alleno, A. Piarristeguy, A. Pradel, A.P. Goncalves, E.B. Lopes, C. Candolfi, A. Dauscher, B. Lenoir, Low-temperature transport properties of Bi-substituted β-As2Te3 compounds, J. Electron. Mater. 45 (2016) 1786–1791.
[31] J.B. Vaney, J.-C. Crivello, C. Morin, G. Delaizir, J. Carreaud, A. Piarristeguy, J. Monnier, E. Alleno, A. Pradel, E.B. Lopes, A.P. Goncalves, A. Dauscher, C. Candolfi, B. Lenoir, Electronic structure, low-temperature transport and thermodynamic properties of polymorphic β-As2Te3, RSC Adv. 6 (2016) 52048–52057.
[32] C. Morin, S. Corallini, J. Carreaud, J.B. Vaney, G. Delaizir, J.C. Crivello, E.B. Lopes, J.M.A. Piarristeguy, C. Candolfi, V. Nassif, G. Cuello, M. Ribes, A. Pradel, A. P. Goncalves, B. Lenoir, E. Alleno, Polymorphism in thermoelectric As2Te3, Inorg. Chem. 54 (2015) 9936–9947.
[33] R.K. Quinn, Compositional dependence of structural and thermal properties of As-Te amorphous alloys, Mat. Res. Bull. 9 (1974) 803–814.
[34] J.C. Rouland, R. Ollitrault-Fichet, J. Flahaut, J. Rivet, R. Ceolin, The As-Te system: phase diagram and glass separation, Thermochim. Acta 161 (1990) 189–200.
[35] J.-B. Vaney, J. Carreaud, A. Piarristeguy, C. Morin, G. Delaizir, R. Viennois, M. Colas, J. Cornette, E. Alleno, J. Monnier, M. Bigot, A.P. Gonçalves, E.B. Lopes, G.J. Cuello, V. Nassif, C. Candolfi, B. Lenoir, A. Pradel, Stabilization of metastable thermoelectric crystalline phases by tuning the glass composition in the Cu–As–Te system, Inorg. Chem. 57 (2018) 754–767.
[36] G. Delaizir, A. Piarristeguy, O. Masson, A. Bouzid, Short range order and network connectivity in amorphous AsTe3: a first principles, machine learning, and XRD study, Phys. Chem. Chem. Phys. 22 (2020) 24895–24906.
[37] J.B. Vaney, G. Delaizir, E. Alleno, O. Rouleau, A. Piarristeguy, J. Monnier, C. Godart, M. Ribes, R. Escalier, A. Pradel, A.P. Gonçalves, E.B. Lopes, G.J. Cuello, P. Ziolkowski, E. Müller, C. Candolfi, A. Dauscher, B. Lenoir, A comprehensive study of the crystallization of Cu–As–Te glasses: microstructure and thermoelectric properties, J. Mater. Chem. A 1 (2013) 8190–8200.
[38] J.D. Musgraves, J. Hu, L. Calvez, Handbook of glass, Springer, 2019.
[39] A. Pradel, T. Pagnier, M. Ribes, Effect of rapid quenching on electrical properties of lithium conductive glasses, Solid State Ion. 17 (1985) 147.
[40] T. Ozawa, Kinetic analysis of derivative curves in thermal analysis, J. Therm. Anal. 2 (1970) 301–324.
[41] E. Alleno, D. Bérardan, C. Byl, C. Candolfi, R. Daou, R. Decourt, E. Guilmeau, S. Hébert, J. Hejtmanek, B. Lenoir, P. Masschelein, V. Ohorodnichuk, M. Pollet, S. Populoh, D. Ravot, O. Rouleau, M. Soulier, A round robin test of the uncertainty on the measurement of the thermoelectric dimensionless figure of merit of Co0.97Ni0.03Sb3, Rev. Sci. Instrum. 86 (2015) 011301.
[42] J. Cornet, D. Rossier, Properties and structure of As-Te glasses: (I). Glass-forming ability and related properties, J. Non-Cryst. Solids 12 (1973) 61–84.
[43] S. Cadars, O. Masson, J.-P. Laval, F.S. Mohammed, A. Piarristeguy, G. Delaizir, A. Bouzid, Insights into the structural complexity and local disorder of crystalline AsTe3 from Semi-Automated First-Principles Modeling", (n.d.).
[44] D. An, S. Zhang, X. Zhai, W. Yang, R. Wu, H. Zhang, W. Fan, W. Wang, S. Chen, O. Cojocaru-Mirédin, X.-M. Zhang, M. Wuttig, Y. Yu, Metavalently bonded tellurides: the essence of improved thermoelectric performance in elemental Te, Nat. Commun. 15 (2024) 3177, https://doi.org/10.1038/s41467-024-47578-w.
[45] R. Vilaplana, S. Gallego-Parra, E.L. Silva, D. Martínez-García, G. Delaizir, A. Muñoz, P. Rodríguez-Hernández, V.P. Cuenca-Gotor, J.A. Sans, C. Popescu, A. Piarristeguy, F.J. Manjón, Experimental and theoretical study of β-As2Te3 under hydrostatic pressure, J. Mater. Chem. C 11 (2023) 1037–1055.
[46] V.P. Cuenca-Gotor, J.A. Sans, J. Ibáñez, C. Popescu, O. Gomis, F.J. Manjón, A. Leonardo, E. Sagasta, A. Suárez-Alcubilla, I.G. Gurtubay, M. Mollar, A. Bergara, Structural, vibrational, and electronic study of α-As2Te3 under compression, J. Phys. Chem. C 120 (2016) 19340–19352.
[47] B.H. Torrie, Raman spectrum of tellurium, Solid State Commun. 8 (1970) 1899–1901.
[48] S. Khatun, A. Banerjee, A.J. Pal, Nonlayered tellurene as an elemental 2D topological insulator: experimental evidence from scanning tunneling spectroscopy, Nanoscale 11 (2019) 3591.
[49] Y. Bouyrie, C. Candolfi, S. Pailhès, M.M. Koza, B. Malaman, A. Dauscher, J. Tobola, O. Boisron, L. Saviot, B. Lenoir, From crystal to glass-like thermal conductivity in crystalline minerals, Phys. Chem. Chem. Phys. 17 (2015) 19751.
[50] S. Misra, C. Barreteau, J.-C. Crivello, V.M. Giordano, J.-P. Castellan, Y. Sidis, P. Levinský, J. Hejtmánek, B. Malaman, A. Dauscher, B. Lenoir, C. Candolfi, S. Pailhès, Reduced phase space of heat-carrying acoustic phonons in single-crystalline InTe, Phys. Rev. Res. 2 (2020) 043371.
[51] C.H. Lee, I. Hase, H. Sugawara, H. Yoshizawa, H. Sato, Low-lying optical phonon modes in the filled skutterudite CeRu4Sb12, J. Phys. Soc. Jpn 75 (2006) 123602.
[52] H. Euchner, S. Pailhès, L.T.K. Nguyen, W. Assmus, F. Ritter, A. Haghighirad, Y. Grin, S. Paschen, M. Boissieu, Phononic filter effect of rattling phonons in the thermoelectric clathrate Ba8Ge40+xNi6−x, Phys. Rev. B 86 (2012) 224303.
[53] M. Schrade, K. Berland, S.N.H. Eliassen, The role of grain boundary scattering in reducing the thermal conductivity of polycrystalline XNiSn (X = Hf, Zr, Ti) half-Heusler alloys, Sci. Rep. 7 (2017) 13760.